Two-dimensional modeling of a polymer electrolyte membrane fuel cell with long flow channel. Part II. Physics-based electrochemical impedance analysis

Cheng Bao [1,3†], Wolfgang G. Bessler [2,3]

1. Department of Thermal Science and Energy Engineering, School of Mechanical Engineering, University of Science & Technology Beijing, Beijing, 100083, P.R. China

2. Institute of Energy System Technology (INES), Offenburg University of Applied Sciences, Badstrasse 24, 77652 Offenburg, Germany

3. German Aerospace Center (DLR), Institute of Technical Thermodynamics, Pfaffenwaldring 38-40, 70569 Stuttgart, Germany

Abstract:

The state-of-the-art electrochemical impedance spectroscopy (EIS) calculations have not yet started from fully multi-dimensional modeling. For a polymer electrolyte membrane fuel cell (PEMFC) with long flow channel, the impedance plot shows a multi-arc characteristic and some impedance arcs could merge. By using a step excitation/Fourier transform algorithm, an EIS simulation is implemented for the first time based on the full 2D PEMFC model presented in the first part of this work. All the dominant transient behaviors are able to be captured. A novel methodology called 'configuration of system dynamics', which is suitable for any electrochemical system, is then developed to resolve the physical meaning of the impedance spectra. In addition to

† Corresponding author. Tel: +86-10-62333682, Fax: +86-10-62329145
E-mail: baocheng@mail.tsinghua.edu.cn

the high-frequency arc due to charge transfer, the Nyquist plots contain additional medium/low-frequency arcs due to mass transfer in the diffusion layers and along the channel, as well as a low-frequency arc resulting from water transport in the membrane. In some case, the impedance spectra appear partly inductive due to water transport, which demonstrates the complexity of the water management of PEMFCs and the necessity of physics-based calculations.

Keywords: Polymer electrolyte membrane fuel cell (PEMFC), electrochemical impedance spectroscopy (EIS), configuration of system dynamics, multi-arc characteristic

1. Introduction

The polymer electrolyte membrane fuel cell (PEMFC) is a key technology for electrochemical energy conversion. One of the crucial subjects of ongoing research and development is the dynamic behavior of the PEMFC. Dynamics plays a key role not only for the application (e.g., required fast load changes for automotive traction), but particularly in the context of cell ageing, where dynamic operation was observed to strongly accelerate degradation [1]. Understanding and optimizing the dynamics of electrochemistry and transport is therefore important for the further development of fuel cell technology.

Electrochemical impedance spectroscopy (EIS) is a classical tool for the dynamic analysis and fault diagnosis of PEMFCs, providing more detailed information than the conventional voltage-current characteristics. The AC impedance studies in PEMFCs have been summarized in the recent reviews [2,3]. The state-of-the-art EIS calculation is based on physical mechanisms rather than conventional equivalent circuit models [4]. With arbitrary input and output signals not limited to cell voltage and current, the physics-based impedance spectroscopy calculation allows generating the so-called transfer function in control theory. Springer et al [5] firstly discussed the

characterization of PEMFC using impedance spectroscopy calculation based on a 1D physicochemical model. However, Schneider et al [6] recently suggested in experiments the existence of an additional low-frequency impedance arc due to the along-the-channel distribution of oxygen concentration, demonstrating the necessity of EIS calculation based on multi-dimensional modeling. It is predictable that this effect will be significant in a PEMFC with long flow channel. Considering this point, Kulikovsky [7] calculated the local impedance of segmented cells based on a qausi-2D model. Using a pseudo-2D approach, Mainka et al [8] discussed the effect of oxygen depletion along the air channel on the Warburg diffusion impedance. By using a sinusoidal excitation of input signal at each frequency point, such EIS calculations were implemented frequency by frequency. Therefore, there are so far no EIS calculations starting from fully multi-dimensional modeling due to limitation of the computational cost.

There are various transient behaviors in PEMFCs, including dynamics of charge transfer in electric double layer (EDL), fluid dynamics in flow channels, dynamics of mass transfer in gas diffusion layer (GDL), dynamics of water transport in the membrane, etc. Compared to fast electrochemical reactions, the slow water transport induces complex dynamic behavior. In general, only the dominant dynamics of charge transfer in EDL and mass transfer in GDL were captured in both simulating and experimental impedance studies [5,9-13]. As a result, a typical impedance plot of PEMFCs shows a clear one- or two-arc characteristic and the dynamics of water transport is little recognized due to the small amplitude of its impedance arc. In some cases, one impedance arc is actually a combination of some different dynamics. For example, the dynamics of along-the-channel oxygen depletion and the dynamics of mass transfer in GDL could overlap in some frequency bands. How to distinguish the multi-arc impedance characteristic brings a

challenge to the physics-based impedance spectroscopy calculation.

The aim of the second part of this work (this paper) is to analyze the transient behavior of PEMFCs using AC impedance spectroscopy. Using the advanced algorithm for the rapid computation of EIS based on step-excitation and Fourier transform developed by Bessler [14], we presented the first EIS calculation of PEMFCs based on a full 2D model. In the context of a PEMFC with long flow channel, all the main impedance arcs were captured and recognized. Then we developed a novel methodology to resolve the physical meaning of multiple arcs in impedance plots. The EIS calculations were carried out at three typical points representing different working regions in V-I curve.

2. Background

2.1 Modeling framework

In the coordinate direction normal to the membrane electrode assembly and the coordinate direction along the gas flow channel, a transient 2D model has been developed in the first part of this work [15]. Fig. 1 shows a schematic of modeling domain. On the membrane level, we made a combination of the concentration solution theory and the dilute solution theory by superposing viscous flow on phenomenological equations. On the electrode level, we developed a Butler-Volmer formulation for the electrochemical kinetics of oxygen reduction reaction (ORR) starting from elementary steps. On the cell level, we used uniform governing equations for transport in free and porous flow in the gas channels and GDLs.

Figure 1 should be here

Mass and momentum balance in the gas channels and GDLs is governed by

$$\frac{\partial\left(\varepsilon_{\mathrm{p}}\rho\right)}{\partial t}+\nabla\cdot\left(\rho\mathbf{u}\right)=0$$
$$\frac{\rho}{\varepsilon_{\mathrm{p}}}\left(\frac{\partial\mathbf{u}}{\partial t}+\left(\mathbf{u}\cdot\nabla\right)\frac{\mathbf{u}}{\varepsilon_{\mathrm{p}}}\right)=\nabla\cdot\left[-p\boldsymbol{I}+\frac{\mu}{\varepsilon_{\mathrm{p}}}\left(\nabla\mathbf{u}+\left(\nabla\mathbf{u}\right)^{T}\right)-\frac{2}{3}\frac{\mu}{\varepsilon_{\mathrm{p}}}\left(\nabla\cdot\mathbf{u}\right)\boldsymbol{I}\right]-\frac{\mu}{K}\mathbf{u}+\mathbf{F} \tag{1}$$

where the dependent variables are the density of gas mixture (ρ) and the superficial velocity vector (**u)**. The equation of state for ideal gas is used to close the system.

Species balance in the gas channels and GDLs is governed by

$$\rho\varepsilon_{\mathrm{p}}\frac{\partial\omega_i}{\partial t}+\nabla\cdot\mathbf{J}_i+\rho\left(\mathbf{u}\cdot\nabla\right)\omega_i=0$$
$$\mathbf{J}_i=-\rho\omega_i\sum_k D_{ik}\varepsilon_{\mathrm{p}}^{1.5}\left[\nabla x_k+\frac{1}{p_{\mathrm{A}}}\left(x_k-\omega_k\right)\nabla p_{\mathrm{A}}\right] \tag{2}$$
$$\mathbf{N}_i=\mathbf{J}_i+\rho\mathbf{u}\omega_i,\qquad x_k=\frac{\omega_k}{M_k}\Big/\sum_i\frac{\omega_i}{M_i},\qquad\sum_i\omega_i=1$$

where the dependent variables are the mass fraction of species *i* (ω_i).

Phenomenological equations with diffusive and viscous flow in the PEM is governed by [15]

$$\mathbf{I}=-\kappa\nabla\phi-\frac{\kappa\xi}{F}\left[\frac{RT}{a_{\mathrm{w}}}\nabla a_{\mathrm{w}}+V_{\mathrm{w}}\frac{\Delta p}{l_{\mathrm{m}}}\mathbf{n}_y\right]-c_{+}F\frac{k_{p,\mathrm{m}}}{\mu_{\mathrm{liq,w}}}\frac{\Delta p}{l_{\mathrm{m}}}\mathbf{n}_y$$
$$\mathbf{N}_{\mathrm{w}}=-\frac{\kappa\xi}{F}\nabla\phi-\left(\frac{c_{\mathrm{w}}D_{\mathrm{w,self}}}{RT}+\frac{\kappa\xi^2}{F^2}\right)\left[\frac{RT}{a_{\mathrm{w}}}\nabla a_{\mathrm{w}}+V_{\mathrm{w}}\frac{\Delta p}{l_{\mathrm{m}}}\mathbf{n}_y\right]-c_{\mathrm{w}}\frac{k_{p,\mathrm{m}}}{\mu_{\mathrm{liq,w}}}\frac{\Delta p}{l_{\mathrm{m}}}\mathbf{n}_y \tag{3}$$

$$\nabla\cdot\mathbf{I}=0$$
$$\frac{1}{1+b\lambda}\frac{\rho_{\mathrm{m,dry}}}{EW}\frac{d\lambda}{da_{\mathrm{w}}}\frac{\partial a_{\mathrm{w}}}{\partial t}+\nabla\cdot\mathbf{N}_{\mathrm{w}}=0 \tag{4}$$

where the dependent variables are the electrolyte potential (ϕ) and the water activity (a_{w}). The sorption curve of $\lambda = f(a_{\mathrm{w}})$, the dependence of characteristic variables (ξ, κ, $D_{\mathrm{w,self}}$ and $k_{\mathrm{p,m}}$) on the water uptake (λ), and the detailed definitions of symbols can be referred to the part work of model development [15].

The boundary conditions are as follows. At the inlet of anode and cathode channels, the inlet velocity is given by an equivalent current density (I_{eq}), which is equal to the operating current

density (I_{avg}) multiplied by the stoichiometry. At the outlet of channel, flow is fully developed.

At the ADL/PEM interface

$$\begin{aligned}&\rho(\mathbf{u}\cdot\mathbf{n})=\left(\mathbf{N}_{\mathrm{H_2}}+\mathbf{N}_{\mathrm{H_2O}}\right)\cdot\mathbf{n},\quad \mathbf{N}_{\mathrm{H_2}}\cdot\mathbf{n}=\frac{I}{2F}M_{\mathrm{H_2}},\quad \mathbf{N}_{\mathrm{H_2O}}\cdot\mathbf{n}=N_{\mathrm{w}}M_{\mathrm{H_2O}},\\&\phi=0,\qquad a_{\mathrm{w}}=p_{\mathrm{a}}x_{\mathrm{H_2O,a}}/p_{\mathrm{sat}}\end{aligned}\tag{5}$$

At the CDL/PEM interface

$$\begin{aligned}&\rho(\mathbf{u}\cdot\mathbf{n})=\left(\mathbf{N}_{\mathrm{O_2}}+\mathbf{N}_{\mathrm{H_2O}}+\mathbf{N}_{\mathrm{N_2}}\right)\cdot\mathbf{n},\\&\mathbf{N}_{\mathrm{O_2}}\cdot\mathbf{n}=\frac{i_{\mathrm{c}}}{4F}M_{\mathrm{O_2}},\quad \mathbf{N}_{\mathrm{H_2O}}\cdot\mathbf{n}=-\left(\frac{i_{\mathrm{c}}}{2F}+N_{\mathrm{w}}\right)M_{\mathrm{H_2O}},\quad \mathbf{N}_{\mathrm{N_2}}\cdot\mathbf{n}=0\\&I=i_{\mathrm{c}}-C_{\mathrm{dl,c}}\frac{\partial\eta}{\partial t},\qquad a_{\mathrm{w}}=p_{\mathrm{c}}x_{\mathrm{H_2O,c}}/p_{\mathrm{sat}}\end{aligned}\tag{6}$$

where $C_{dl,c}$ is the area-specific capacity of the cathode-side electric double layer, the cathode-side Faraday's current density (i_c) is given by [15]

$$\begin{aligned}i_{\mathrm{c}}=i_{0,353}\exp&\left[\frac{73.2[\mathrm{kJ\ mol^{-1}}]}{R}\left(\frac{1}{353}-\frac{1}{T}\right)\right]\left(\frac{p_{\mathrm{c}}x_{\mathrm{O_2}}}{RTc_{\mathrm{O_2,ref}}}\right)^{(1-\alpha)/2}a_{+}^{1-2\alpha}\\&\times\left[\exp\left(-\frac{2\alpha F\eta}{RT}\right)-\exp\left(\frac{2(1-\alpha)F\eta}{RT}\right)\right]\end{aligned}\tag{7}$$

where $\eta=V_{\mathrm{cell}}-\phi-V_{\mathrm{eq}}+V_{\mathrm{loss}}$ is the overpotential, in which V_{cell} is the cell voltage, V_{eq} is the equilibrium electrochemical force calculated from Nernst equation, and V_{loss} is the leakage voltage, the activity of solvated proton (hydronium), a_+, is calculated by [15]

$$a_{+}=\frac{(\lambda+1)-\sqrt{(\lambda+1)^2-4\lambda(1-1/K_e)}}{2(1-1/K_e)}\tag{8}$$

where K_e = 166.26 at 353 K.

The coupled nonlinear system contains 11 dependent variables, u_c, v_c, p_c, x_{O2}, x_{H2O} in the cathode, u_a, v_a, p_a, x_{H2} in the anode, and ϕ, a_w in the membrane. All the equations in this model were solved in the commercial environment, COMSOL Multiphysics 4.2a [16] on a desktop

computer with 2 GHz and 8 GB RAM.

With the parameters listed in Table 1, the model has been run at steady state and validated by the complete range of available experimental polarization behavior [17]. The experiments were carried out on a 50 cm^2 single cell with a multi-channel meander flow field at a pressure of 2 bar under coflow mode. A Nafion 112 membrane was used; platinum loading of the electrodes was 0.8 g cm^{-2}. The reference exchange current density ($i_{0,353}$) and transfer coefficient (α) of the ORR, as well as the leakage voltage (V_{loss}), were used as the fitting parameters.

Table 1 should be here

2.2 Rapid impedance calculation

The transient modeling framework presented here allows physically-based impedance simulations without using equivalent circuit models. Different approaches for impedance simulation were presented before, including frequency-response analyzer (FRA)-type sinusoidal excitation and Fourier transform techniques [18,19]. The high numerical cost of sinusoidal excitation technique limits its application in multi-dimensional models as used here. Therefore, we used here a Fourier-transform method based on the transient numerical simulation of a fast, sub-microsecond potential step followed by current relaxation. All the input and output data were obtained in time domain. The impedance was then reconstructed by applying a Fourier transform to the resulting current and potential traces. As a step signal contains, in principle, the complete frequency information, a rapid generation of a complete impedance spectra is possible with a single simulation run.

An exponential step of the cell voltage was used here as

$$V_{\text{cell}}(t) = V_{\text{base}} + \left[1 - \exp\left(-\frac{t}{\tau}\right)\right] V_{\text{step}} \tag{9}$$

where V_{base} is the voltage before the step and V_{step} is the magnitude of the step. As we want to stay within the linear range of the electrochemical system, V_{step} was chosen to be 5 mV. The duration of the step is giving by its characteristic time τ = 10^{-6} s, which is chosen to be small enough to contain high-frequency information and decouple the fastest characteristic time scales of the system from those of excitation and relaxation, improving the numerical stability [14].

For a discrete time series $H(t)$, the corresponding Fourier transform $H^*(\omega)$ at an arbitrary angular frequency ω is defined as

$$H^*(\omega) = \sum_{n=1}^{N} \int_{t_n}^{t_{n+1}} H(t) \exp(-j\omega t)\, dt \tag{10}$$

where the non-equally spaced time steps $\{t_1, \ldots, t_N\}$ are generated automatically by the adaptive solver of COMSOL Multiphysics. We further added an additional artificial data point at $t_{N+1} = 2t_N$ in order to drive the system back to the original state [14]. Between the two given steps $[t_n, t_{n+1}]$, the time function is approached by a linear interpolation as $H(t) = H(t_n)+[H(t_{n+1})-H(t_n)](t-t_n)/(t_{n+1}-t_n)$. The complex frequency-domain electrochemical impedance $Z(\omega)$ is then obtained by

$$Z(\omega) = -V_{\text{cell}}^*(\omega) \big/ I_{\text{avg}}^*(\omega) \tag{11}$$

where the negative sign in the above equation results from the different definitions of positive current in fuel cell operation and electrical engineering.

3. Impedance simulation

Before simulating electrochemical impedance spectra based on our fully 2D model, an exemplary one-dimensional EIS calculation was firstly implemented for comparison with experimental data from Springer et al [5]. Results are shown in Fig. 2. The calculation was carried

out using the Fourier transform technique outlined in Section 2.2. For this simulation, the vapor partial pressure in the cathode was fixed to be the saturation vapor pressure (as assumed by Springer [5]). The logarithmic mean of the inlet and outlet oxygen concentration was taken as the bulk oxygen concentration at the channel/GDL interface [20-23]. Fig. 2 demonstrates a good agreement between model and experiment of the impedance at various cell voltages, thus validating our simulating framework. Note that, the values of the exchange current density, double layer capacitance in Fig. 2 were just used here for this exemplary calculation. In the next calculations, we used the base values in Table 1.

Figure 2 should be here

Next, impedance simulations of the base 2D model were carried out at three typical points representing different working regions in V-I curve. Fig. 3 shows a simulated complex plane (or Nyquist) impedance plot at V_{cell} = 1.049 V, while the open circuit voltage is almost 1.05 V. The frequency range extends between 10^{-3} and 10^{5} Hz. In the region of activation polarization (high frequency), the charge transfer in the double layer dominates the cell impedance. The impedance plot approaches the shape of an ideal semi circle of a typical $(R_{ct}||C_{dl})-R_{ohm}$ equivalent circuit [4], in which the charge-transfer resistance (R_{ct}) corresponds to the diameter of the circle, the ohmic resistance (R_{ohm}) is equal to the impedance at $\omega\rightarrow\infty$, and the characteristic frequency at maximum imaginary is $\omega_m = 1/R_{ct}C_{dl}$. Note that the steady-state charge-transfer resistance of a single charge-transfer reaction is defined as $R_{ct} = d\eta/di = RT/2Fi_0$ via linearization of the exponent terms in Eq. (7) at low overpotential. Corresponding to the estimated cathode exchange current density i_0 = 87.9 A m^{-2}, the value of R_{ct} = 1.73 Ω cm^2 is slightly lower than the diameter of the simulated ideal semi circle, indicating that the impedance includes additional resistances, most likely due to

gas transport. Fig. 3 also shows simulations for a variation of the exchange current density i_0. Results are in agreement as would be extended from the equivalent circuit model. As fuel and air are fully humidified and the membrane is quite thin, R_{ohm} = 0.045 Ω cm^2 is small in this example. Because the cathode-side double layer behaviors are dominant in typical PEMFC operations, we did take the dynamics of the anode-side EDL into account here.

Figure 3 should be here

Fig. 4 shows simulated impedance spectra at V_{cell} = 0.7 V. Under this typically practical PEMFC operation point, the Nyquist plot contains ***three*** arcs. Physically-based impedance modeling allows the direct assessment of the origin of impedance features to physicochemical processes. To this goal, we developed a methodology called '***configuration of system dynamics***', i.e. subsequently modified the governing equations by switching on or off individual transient terms: dynamics of the charge transfer due to the double layer capacitor ($C_{dl}\partial\eta/\partial t$), dynamics of the mass transfer and flow in the gas channels and GDLs ($\partial\mathbf{u}/\partial t$, $\partial\rho/\partial t$ and $\partial\omega_i/\partial t$) and dynamics of the water transport in PEM ($\partial a_w/\partial t$ or $\partial\lambda/\partial t$). Corresponding to a unique steady-state behavior of the system, all impedance curves intersect at the same point on the x-axis for low frequencies (i.e. direct-current resistance as $\omega \rightarrow 0$).

By comparing the impedance plots with different combination of dynamic terms, we can easily conclude that the high-frequency arc ('arc 1') represents the transient behavior of double layers. Note that, at least in our example, the charge-transfer arc ('arc 1') in the region of ohmic overpotential in V-I curve is also the largest arc (compared to 'arc 2' and 'arc 3'), although it is not large as that in the region of activation overpotential (cf. Fig. 3).

Figure 4 should be here

In order to identify the smaller ‘arc 2’ and ‘arc 3’, we further investigated the system behaviors without considering the dynamics of the double layer. The results are shown in Fig. 5. As suggested by Schneider’s experiments [6] and Kulikovsky’s local impedance calculation of segmented cells [7], the ‘arc 2’ represents low-frequency impedance due to the along-the-channel oxygen transport. In our example, the large ratio of channel length to depth (L_{ch}/D_{ch} = 928.2) makes this effect strong enough to be clearly visible. However, the Nyquist plot of ‘mass transfer/flow’ also contains two arcs (arc ‘2A’ and ‘2B’ in Fig. 5b). To separate them, we designed two numerical experiments named ‘without GDL’ and ‘without channel’. Technically, the ‘without GDL’ case can be easily realized by setting the porosity and permeability of porous media to be those of a free volume (ε_p = 1 and $K \rightarrow \infty$) and reducing the thickness of GDL. For “removing” the gas channel, the channel/GDL interfaces were set to Dirichlet boundaries and the simpler Darcy’s flow instead of the Navier-Stoke equation was used in the ‘without channel’ case. Due to the lack of parts of the mass transfer resistance, the ‘without GDL’ and ‘without channel’ spectra have smaller maximum real impedance (i.e. direct-current resistance as $\omega \rightarrow 0$) than that of the ‘mass transfer/flow’ spectrum. However, by comparing among the radius, shape and characteristic frequencies of these three impedance plots as shown in Fig. 5b, we can uniquely identify the arc ‘2A’ and ‘2B’ due to the mass transfer in GDLs and along-the-channel transport, respectively.

The comparison between the ‘mass transfer/flow + water’ and ‘water’ spectra, i.e. the arc shape qualitatively and the characteristic frequency quantitatively, shows that the ‘arc 3’ results from the dynamics of water transport in the membrane. It is interesting that the ‘water’ spectrum also contains two arcs (arc ‘3A’ and ‘3B’ in Fig. 5b). Similarly, we designed the ‘water, without channel’ simulation, whose impedance curve contains basically a single arc (a little distort at high

frequency should result from transport in GDL) like the arc '3B'. At this point, we considered the arc '3A' is due to the water vapor transport along the channel. As shown in Fig. 5b, the 'mass transfer/flow + water' spectrum contains three arcs, i.e. the 'water' arc at low frequency, 'transport along the channel' arc at medium frequency and 'transport in GDL' arc at relatively high frequency. When the complete dynamics was considered, the small 'transport in GDL' arc is almost merged by the big 'charge transfer' arc (cf. Fig. 4b). The frequency sequence of these three arcs can also be roughly estimated by their characteristic time constants.

$$\tau_{\mathrm{ch}} = \frac{L_{\mathrm{ch}}}{u_{\mathrm{in,c}}} = \frac{4Fp_{\mathrm{c,in}}x_{\mathrm{O_2,in}}D_{\mathrm{ch,c}}}{I_{\mathrm{eq,c}}RT}, \quad \tau_{\mathrm{GDL}} = \frac{l_{\mathrm{c}}^2}{D_{\mathrm{O_2,H_2O}}\varepsilon_{\mathrm{P}}^{1.5}}, \quad \tau_{\mathrm{w}} = \frac{l_{\mathrm{m}}^2}{D_{\mathrm{w,Fick}}} \tag{12}$$

With $D_{\mathrm{O2,H2O}}$ = 1.868×10^{-5} m^2 s^{-1}, $D_{\mathrm{w,Fick}}$ = 5.88×10^{-10} m^2 s^{-1} [24] and other parameters in Table 1, there are τ_{ch} = 0.213 s, τ_{GDL} = 0.019 s and τ_{w} = 4.25 s, i.e. $\tau_{\mathrm{GDL}} < \tau_{\mathrm{ch}} < \tau_{\mathrm{w}}$ consistent with the frequency sequence of arc '2A', '2B' and 'arc 3' in our example.

Figure 5 should be here

Figure 6 shows the impedance plots at V_{cell} = 0.4 V. At this time, the cell operates in a region close to transport limitation, i.e. the region of concentration overpotential in V-I curve. The spectrum with complete dynamics again contains three arcs. However, the origin of these three arcs is different from that at V_{cell} = 0.7 V (Fig. 4b). By comparing impedance plots with different combination of dynamics, we could assign 'arc 1' to charge transfer, 'arc 2' to transport in GDL, and 'arc 3' to transport along the channel. Because mass transfer dominates the polarization loss at this operating point, the 'transport along the channel' arc and even the 'transport in GDL' arc become larger than the 'charge transfer' arc. Kulikovsky et al. [7] also suggested that the radius of transport arc increases as oxygen concentration decreases along the channel. As a result, the small

‘water transport in PEM’ arc is absorbed by the large arc due to mass transfer.

Figure 6 should be here

Figure 7 shows simulated impedance spectra for dry reactants (RH = 0.1) at different flow modes and fuel flow rates (I_{eq}). As discussed in the steady-state simulation [15], the counterflow operation is helpful to making internal humidification for partly humidified fuel and air, especially for fuel cells with a long gas channel. See also Fig. 7, the counterflow mode reduces the ohmic loss (corresponding to the point with minimum real impedance) and the overall loss (the point with maximum real impedance) as compared to coflow mode. At high anode stoichiometry in the counterflow mode (case 4), the good internal humidification results in a three-arc impedance similar to that of fully-humidified reactants (cf. Fig. 4 and 5). In other cases (case 1-3), the simulations show low-frequency arcs with positive imaginary part, which means an inductive characteristics of water transport in the membrane. The complexity of impedance spectra at different operating conditions demonstrates the necessity of physically-based modeling.

Figure 7 should be here

We consider the inductive behavior to be attributed to the diffusion flux of water, or water-uptake gradient, across the membrane. To validate this point, we carried out two simulations with varying membrane thickness. As shown in Fig. 8, a significant inductive arc appears in the ‘175 μm’ calculation, while it diminishes in the ‘10 μm’ calculation. For the thinner membrane, more intensive back-diffusion water flux helps to decelerate the phase-angle lead of the membrane resistance. This can also explain the results in the ‘case 4’ in Fig. 7, where inductive arc does not appear due to the strengthened self-humidification with higher anode flow rate under counterflow

mode.

Figure 8 should be here

4. Conclusions

Due to limitation of the computational cost, the state-of-the-art physics-based EIS calculations have not yet started from fully multi-dimensional modeling. In a typical impedance plot of PEMFCs, the dynamics of water transport in PEM is little captured and recognized due to the small amplitude of its impedance arc. For a PEMFC with long flow channel, the additional transient behavior due to the along-the-channel oxygen depletion makes a multi-arc impedance characteristic, which brings a challenge to be resolved in physics-based EIS calculation.

Based on a step excitation/Fourier transform algorithm, we implemented a simulation for the first time electrochemical impedance spectra based on a multi-physics full 2D PEMFC model. All the dominant transient behaviors, including the dynamics of water transport in PEM, are able to be captured. A methodology called 'configuration of system dynamics' by tailoring the transient terms in the governing equations, was then developed to identify the physical meaning of the impedance spectra. At low current density (activation region), the charge transfer process in the cathode dominates the impedance plot, which approaches to a single feature in the form of an ideal semi circle. At intermediate current density (region of ohmic loss), the impedance plot show a three-arc characteristic: A high-frequency arc due to charge transfer in the double layer, a medium-frequency arc due to transport along the channel and GDL, and a low-frequency arc due to water transport in the membrane. At high current density (region of concentration loss), the impedance plot again shows a multi-arc feature. However, the 'along-the-channel transport' arc and even the 'mass transfer in GDL' arc are larger than the 'charge transfer' arc, while the small

‘water transport’ arc is masked by the other features. By using dry reactants with suitable stoichiometries, the effective internal humidification in the counterflow mode resulted in a three-arc impedance plot similar to that of full humidification. However, the impedance spectra in some cases appear partly inductive due to water transport, which demonstrates the complexity of the water management of PEMFCs and the necessity of physics-based calculations.

Note that the methodology of ‘configuration of system dynamics’ is suitable for any electrochemical system, not limited to the context of fuel cell. The present computational approach allows the study of arbitrary transient input and output signals, which can be used, for example, for system identification and controller design.

There are several open topics to be treated in future studies. Firstly, the present model assumes single-phase water transport [15], which does not include behaviors of drops, slugs and flooding and the resulting complex transient performance [25]. Secondly, the simulated faradic impedance arcs appear as ‘perfect’ semi-circles, while impedance arcs originating from charge transfer and double layer often experimentally show a ‘depressed’ shape. The origin of the depression is usually accounted to a spatially inhomogeneous electrochemical activity due to spatially distributed reactant concentration and electrical potential [4]. In the present modeling approach, the catalyst layers are treated as flat boundaries between GDL and membrane. Therefore, simulated impedance arcs appear as “perfect” semi-circles. Note that concentration inhomogeneities in the gas transport layers (channels, GDLs) alone, although providing inhomogeneous boundary conditions to the catalyst layer, do not lead to depressed charge-transfer arcs, as has been shown before by Bessler in the context of solid oxide fuel cells [26][27]. We believe that a microstructural model of the catalyst layer is required in order to capture the depressed-arc behavior. Thirdly, the

low-frequency inductive loops are typically attributed to the adsorbate dynamics in the chain of the ORR events. As shown in Fig. 8a, inductive arcs appear at quite low characteristic frequency (0.016 Hz). In the present modeling approach, we used the water absorption curve, $\lambda = f(a_w)$, for transient process, i.e. assuming water in the PEM/GDL boundary in thermodynamic equilibrium at any time. In reality, the membrane-water system could reach equilibrium by days and therefore inductive arcs might not appear or be distinguished experimentally. Finally, the impedance simulations take too long to be directly applicable for control or diagnostic applications, which normally require real-time performance. As for the exploitability of our approach, Bao previously implemented frequency-domain analysis of a PEM fuel cell system configured with anode recirculation and introduced the concept of active anode purge for water management [28].

Acknowledgement

CB acknowledges the Alexander von Humboldt Foundation for granting a fellowship for experienced researchers. WGB acknowledges support from the Initiative and Networking fund of the Helmholtz Association.

Nomenclature

a	Activity
b	Swelling factor of membrane, b = 0.0126
C_{dl}	Area-specific capacity of double layer (F m^{-2})
D	Diffusivity (m^2 s) or channel depth (m)
F	Faraday's constant (96485 C mol^{-1})

i_0	Exchange current density (A m^{-2})
i	Faradic current density (A m^{-2})
I	Current density (A m^{-2})
J	Diffusive molar flux (mol $m^{-2}s^{-1}$)
$k_{p,m}$	Hydraulic permeability in the membrane
K	Hydraulic permeability in GDL (m^2), $K \rightarrow \infty$ in gas channels
l	Thickness (m)
L_{ch}	Channel length (m)
N	Total molar flux (mol m^{-2} s^{-1})
p	Pressure (Pa)
R	Universal gas constant (8.314 J mol^{-1} K^{-1})
RH	Relative humidity
T	Temperature (K)
u, v	Velocity (m s^{-1})
V	Partial molar volume (m^3 mol^{-1}) or voltage (V)
x	Molar fraction
y, z	Coordinates in the direction of thickness and length (m)
Re(Z), Im(Z)	Real and imaginary part of complex impedance Z (Ω m^2)

Greek

α	Anodic transfer coefficient
β	Net water transport coefficient

ε_p	Porosity, $\varepsilon_p = 1$ in gas channels
η	Overpotential (V)
ϕ	Electrolyte potential (V)
κ	Membrane conductivity (S m^{-1})
λ	Water uptake in the membrane (H_2O/R-SO_3H)
μ	Dynamic viscosity (Pa s)
ξ	Electro-osmotic drag coefficient
ρ	Density (kg m^{-3})
ω	Mass fraction or angular frequency (rad s^{-1})

Subscripts and superscripts

a	Anode
avg	Average or overall
c	Cathode
H_2O	Water vapor in gas channel or GDL
i, j	Species
in	Inlet
m	Membrane
w	Water in the membrane
+	Proton

Figure and Table Captions

- Fig. 1: Schematic of the two-dimensional modeling domain.

- Fig. 2: Exemplary 1D calculations and measurements of impedance at various cell voltages on an experimental cell with 300 μm cathode, Nafion 115 membrane and operated at 5 atm air, 3 atm H_2. Fuel and air are both fully humidified and cathode flow rate is 500 sccm. Fitted parameters are: uniform Tafel slope of 85 mV/decade, cathode porosity of 0.4, tortuosity of 6.5, and the area-specific double layer capacity of 81.9, 76.8 and 168 F m^{-2} at 0.81, 0.77 and 0.48 V, respectively.
- Fig. 3: Nyquist plots under the condition of full humidification and coflow mode at V_{cell} = 1.049 V. Other parameters are identical to those in Table 1.
- Fig. 4: (a) Bode plots and (b) Nyquist plots with different configuration of model dynamics under the condition of full humidification and coflow mode at V_{cell} = 0.7 V. Other parameters are identical to those in Table 1.
- Fig. 5 (a) Bode plots and (b) Nyquist plots with different configuration of model dynamics to identify 'arc 2' and 'arc 3' in Fig. 4.
- Fig. 6: (a) Bode plots and (b) Nyquist plots with different configuration of model dynamics under the condition of full humidification and coflow mode at V_{cell} = 0.4 V. Other parameters are identical to those in Table 1.
- Fig. 7: Impedance plots for different flow modes and fuel stoichiometries using dry reactants, RH_a = 0.1, RH_c = 0.1, V_{cell} = 0.7 V, $I_{eq,c}$ = 4×10^3 A m^{-2}, case 1: $I_{eq,a}$ = 2.2×10^3 A m^{-2} and coflow, case 2: $I_{eq,a}$ = 2.2×10^3 A m^{-2} and counterflow, case 3: $I_{eq,a}$ = 1.0×10^4 A m^{-2} and coflow, case 4: $I_{eq,a}$ = 1.0×10^4 A m^{-2} and counterflow. Other parameters are identical to those in Table 1.
- Fig. 8: Impedance plots of dry operation for different membrane thickness, (a) l_m = 175 μm and (b) l_m = 10 μm. Parameters are identical to those of 'case 1' in Fig. 7.

- Table 1: Main parameters in base case.

References

[1] A.A. Franco. PEMFC degradation modeling and analysis, in: C. Hartnig, C. Roth (Eds.) Polymer electrolyte membrane and direct methanol fuel cell technology (PEMFCs and DMFCs), CRC press (2012).

[2] X.Z. Yuan, H.J. Wang, J.C. Sun, J.J. Zhang, Int. J. Hydrogen Energy 32 (2007) 4365-4380.

[3] S.M.R. Niya, M. Hoorfar, J. Power Sources 240 (2013) 281-293.

[4] E. Barsoukov, J.R. Macdonald, Impedance spectroscopy. Theory, experiment and applications (second edition), John Wiley & Sons, New York (2005).

[5] T. E. Springer, T. A. Zawodzinski, M. S. Wilson and S. Gottesfeld, J. Electrochem. Soc. 143 (1996) 587-599.

[6] A. Schneider, S.A. Freunberger, D. Kramer, A. Wokaun, G.G. Scherer, J. Electrochem. Soc. 154 (2007) B383-B388.

[7] A. Kulikovsky, A model for local impedance of a PEM fuel cell with segmented electrodes. 9th Symposium on fuel cell and battery modeling and experimental validation (ModVal9), Sursee, Switzerland, 2-4, April (2012).

[8] J. Mainka, G. Maranzana, J. Dillet, S. Didierjean, O. Lottin, J. Electrochem. Soc. 157 (2010) B1561-B1568.

[9] M.A. Rubio, A. Urquia, R. Kuhn, S. Dormido, J. Power Sources 183 (2008) 118-125.

[10] A. Hakenjos, C. Heling, J. Power Sources 145 (2005) 307-311.

[11] M.U. Iftikhar, D. Riu, F. Druart, S. Rosini, Y. Bultel, N. Retiere, J. Power Sources 160 (2006) 1170-1182.

[12] J.O. Rourke, M. Ramani, M. Arcak, Int. J. Hydrogen Energy 33 (2008) 4694-4701.

[13] W. Merida, D.A. Harrington, J.M. Le canut, G. McLean, J. Power Sources 161 (2006) 264-274.

[14] W.G. Bessler, J. Electrochem. Soc. 154 (2007) B1186-B1191.

[15] C. Bao, W.G. Bessler, Two-dimensional modeling of a polymer electrolyte membrane fuel cell with long flow channel - I. Model development. Accepted by J. Power Sources. 2014

[16] COMSOL Multiphysics 4.2a, http://www.comsol.com

[17] M.P. Eschenbach, R. Coulon, A.A. Franco, J. Kallo, W.G. Bessler, Solid State Ionics 192 (2011) 615-618.

[18] W.G. Bessler, Solid State Ionics 176 (2005) 997-1011.

[19] Y.X. Shi, N.S. Cai, C. Li, C. Bao, E. Croiset, Q. Hu, J.Q. Qian, S.R. Wang, J. Electrochem. Soc. 153 (2008) B270-280.

[20] C. Bao, M.G. Ouyang, B.L. Yi, Int. J. Hydrogen Energy 31 (2006) 1879-1896.

[21] C. Bao, M.G. Ouyang, B.L. Yi, J. Power Sources 156 (2006) 232-243.

[22] C. Bao, M.G. Ouyang, B.L. Yi, Int. J. Hydrogen Energy 31 (2006) 1040-1057.

[23] C. Bao, W.G. Bessler, J. Power Sources 210 (2012) 67-80.

[24] S. Motupaly, A.J. Becker, J.W. Weidner, J. Electrochem. Soc. 147 (2000) 3171-3177.

[25] E. Kimball, T. Whitaker, Y.G. Kevrekidis, J.B. Benziger, AIChE J. 54 (2008) 1313-1332.

[26] W.G. Bessler, J. Electrochem. Soc. 153 (2006) A1492-A1504.

[27] W.G. Bessler, S. Gewies, J. Electrochem. Soc. 154 (2007) B548-B559.

[28] C. Bao, M.G. Ouyang, B.L. Yi, Int. J. Hydrogen Energy 31 (2006) 1897-1913.

Table 1

Table 1 Main parameters in base case

Meaning	Symbol	Value
Thickness of anode diffusion layer (m)	l_a	3.0×10^{-4}
Thickness of cathode diffusion layer (m)	l_c	3.0×10^{-4}
Thickness of PEM (m)	l_m	5×10^{-5}
Depth of anode gas channel (m)	$D_{ch,a}$	1×10^{-3}
Depth of cathode gas channel (m)	$D_{ch,c}$	1×10^{-3}
Channel length (m)	L_{ch}	0.9282
Anode gas pressure (Pa)	p_a	2.026×10^{5}
Cathode gas pressure (Pa)	p_c	2.026×10^{5}
Cell temperature (K)	T	353
Anode inlet gas relative humidity (%)	RH_a	100
Cathode inlet gas relative humidity (%)	RH_c	100
Anode equivalent current density (A m^{-2})	$I_{eq,a}$	2×10^{4}
Cathode equivalent current density (A m^{-2})	$I_{eq,c}$	2×10^{4}
Area-specific capacitor of cathode electric double layer (F m^{-2}) [9]	$C_{dl,c}$	25.0
Cathode exchange current density at 353 K (A m^{-2}) ‡	$i_{0,353}$	150
Transfer coefficient of the overall ORR ‡	α	0.18
Leakage voltage (V) ‡	V_{loss}	0.1417
Flow mode		coflow

‡ fitted

Figure 1
Click here to download high resolution image

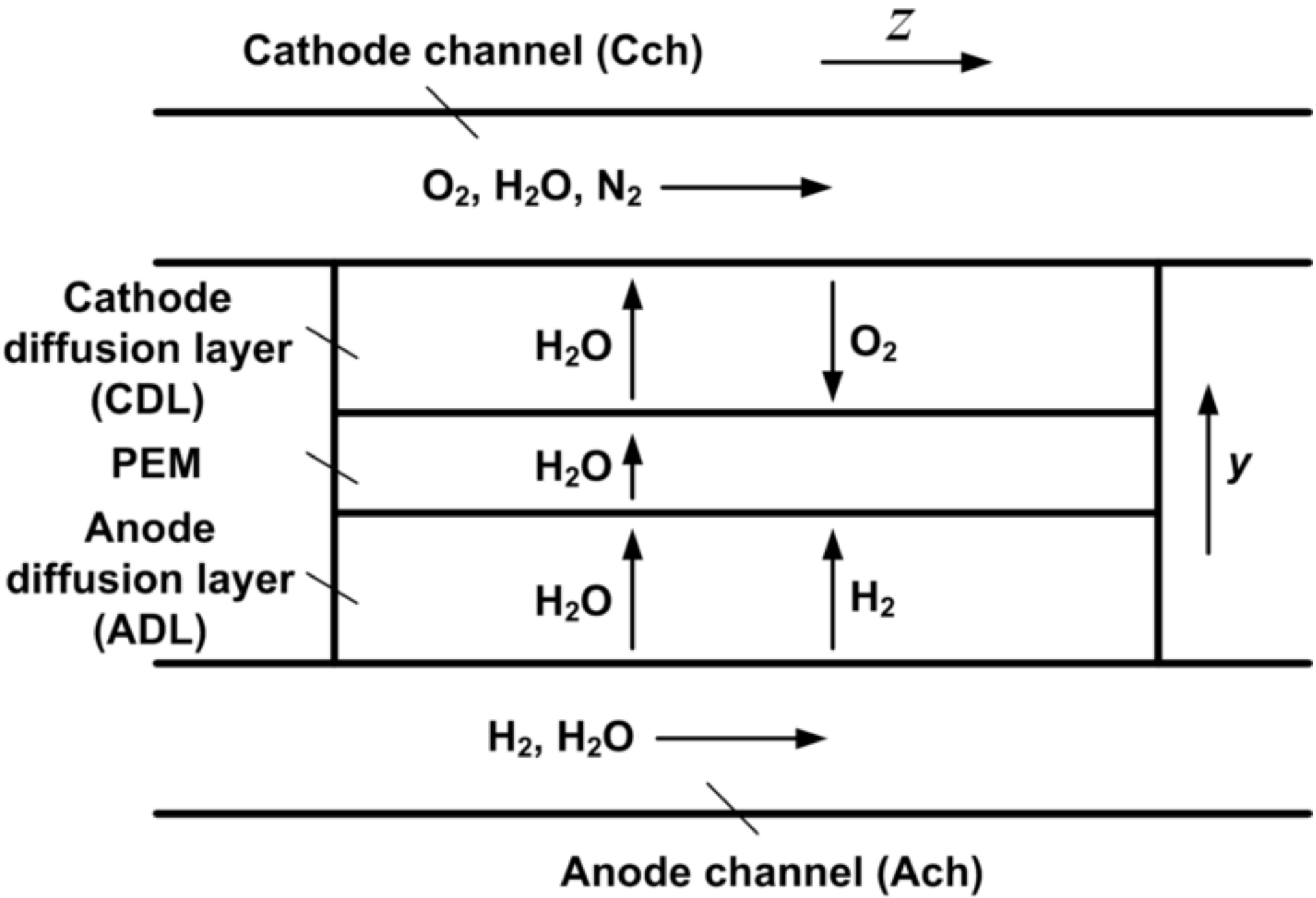

Figure 2

Click here to download high resolution image

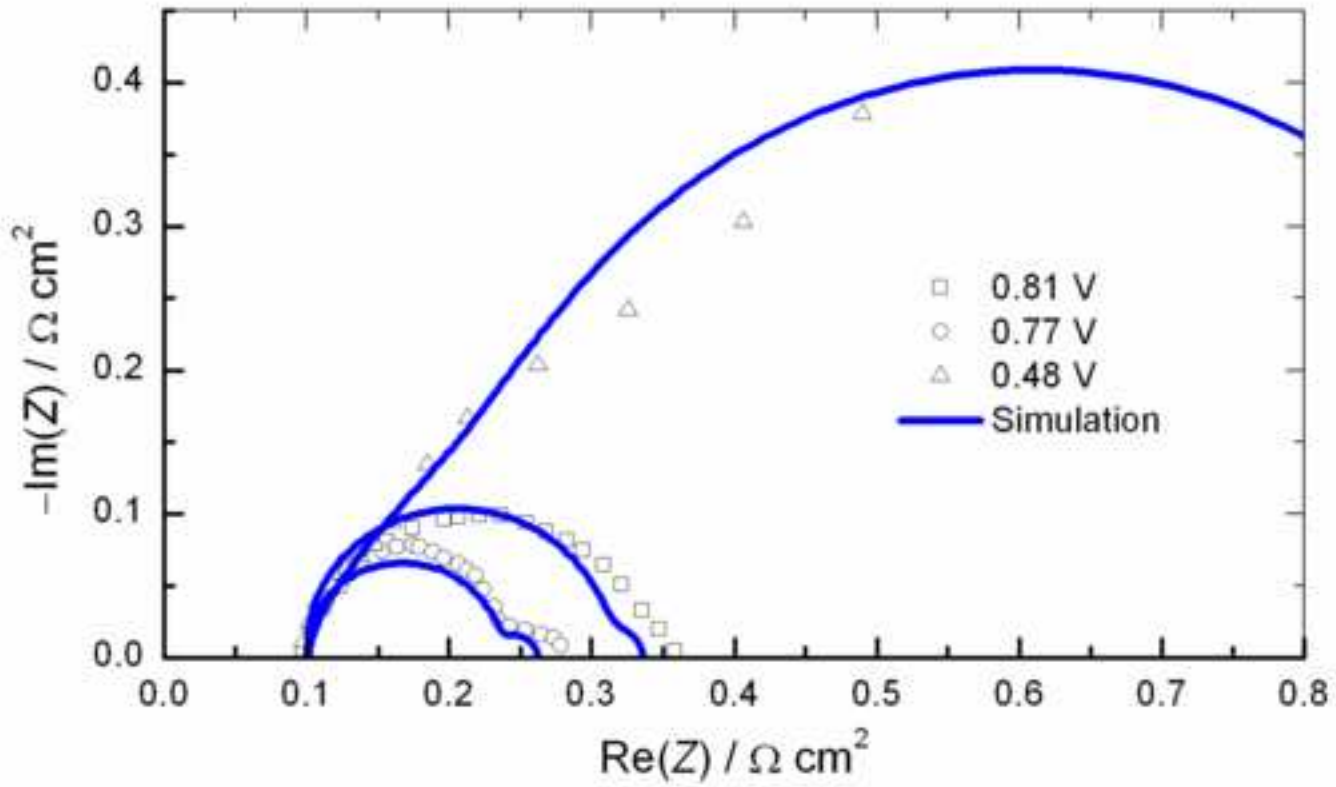

Figure 3

Click here to download high resolution image

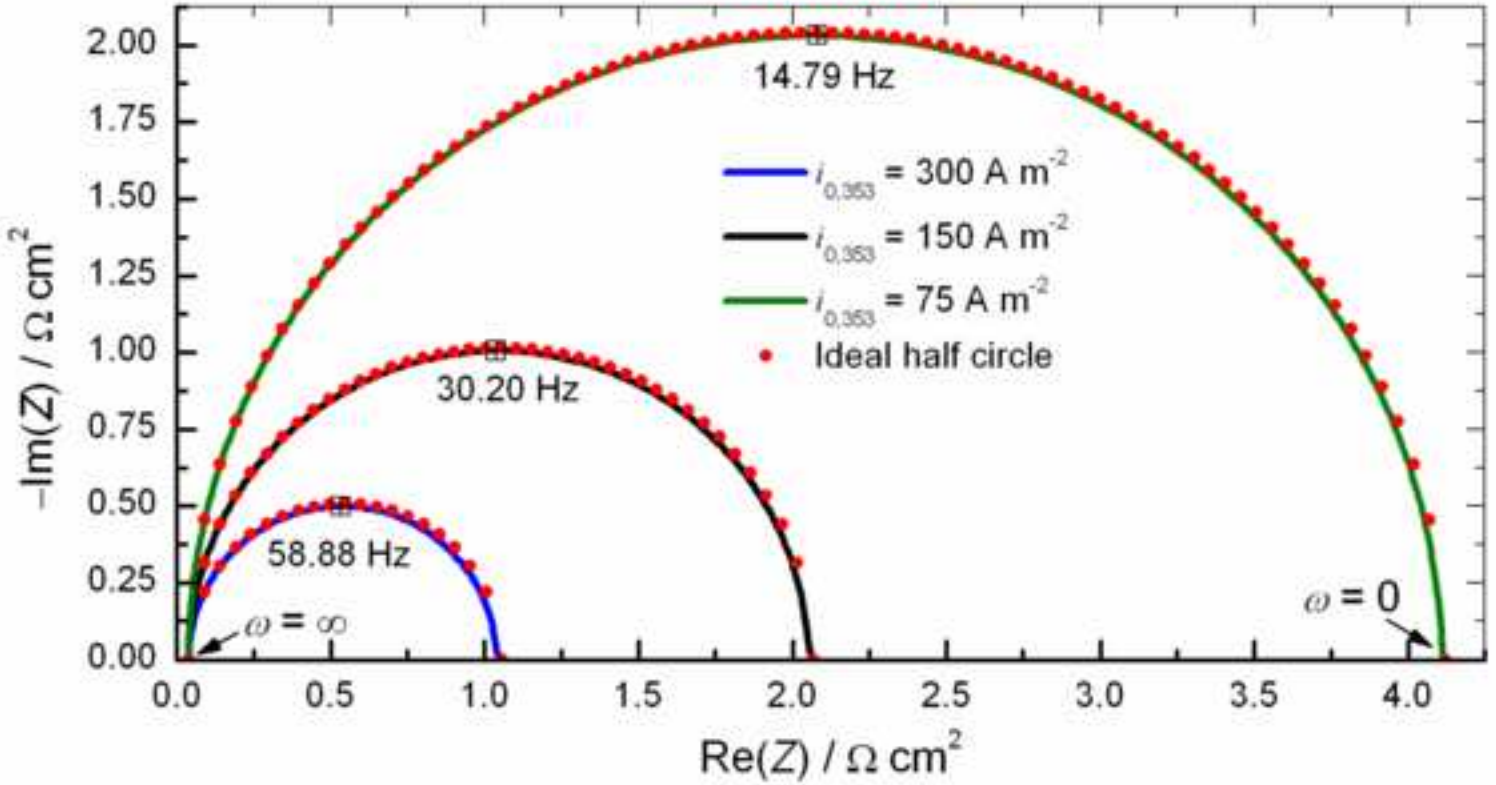

Figure 4a

Click here to download high resolution image

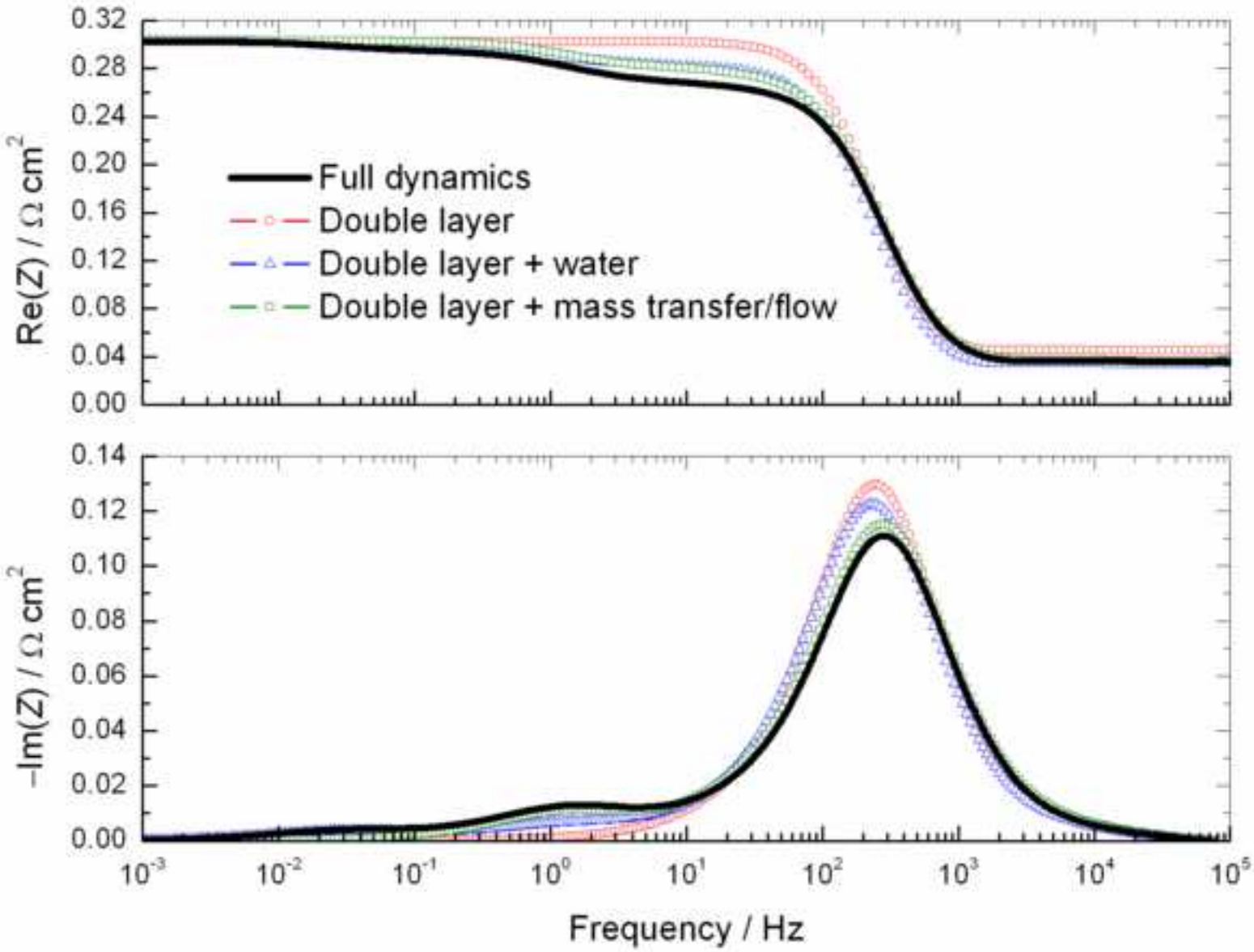

Figure 4b

Click here to download high resolution image

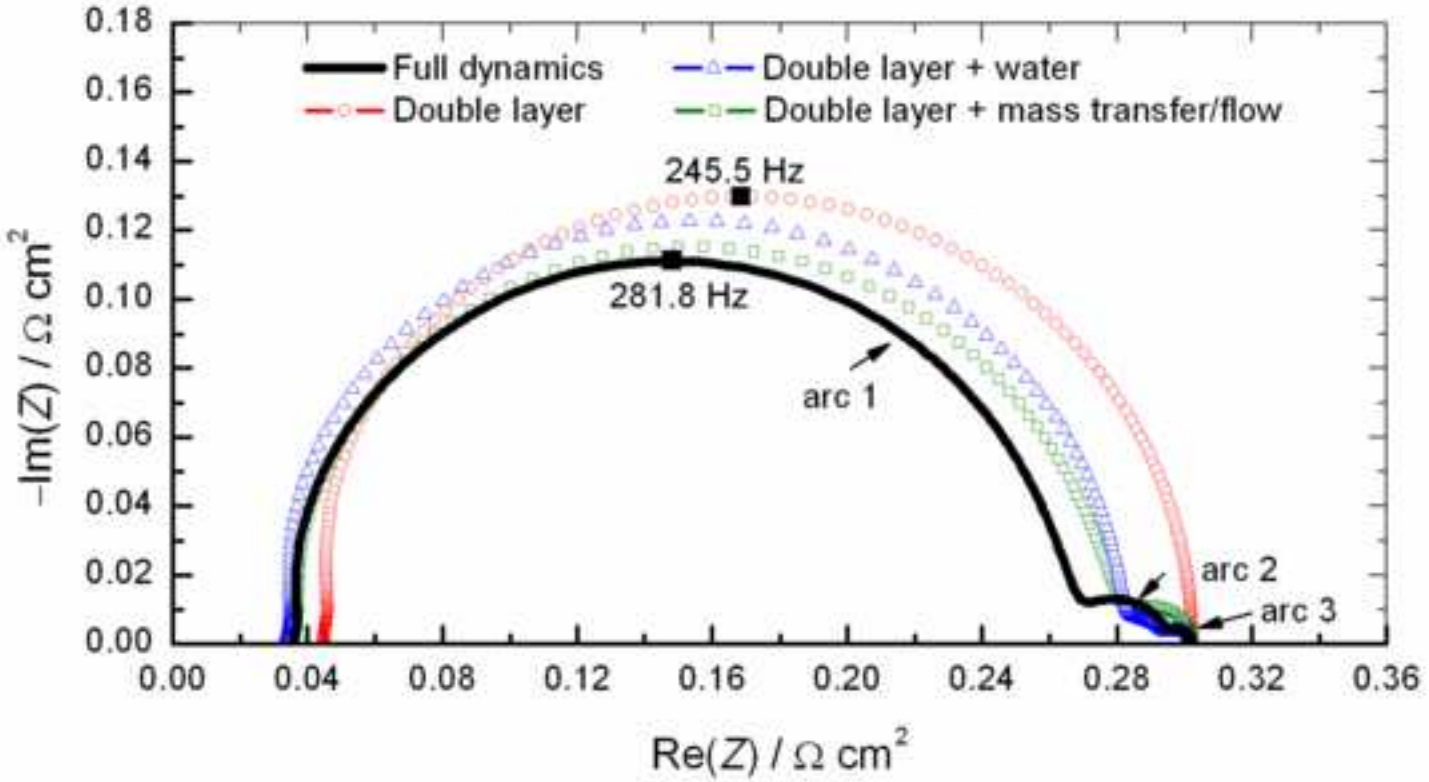

Figure 5a

Click here to download high resolution image

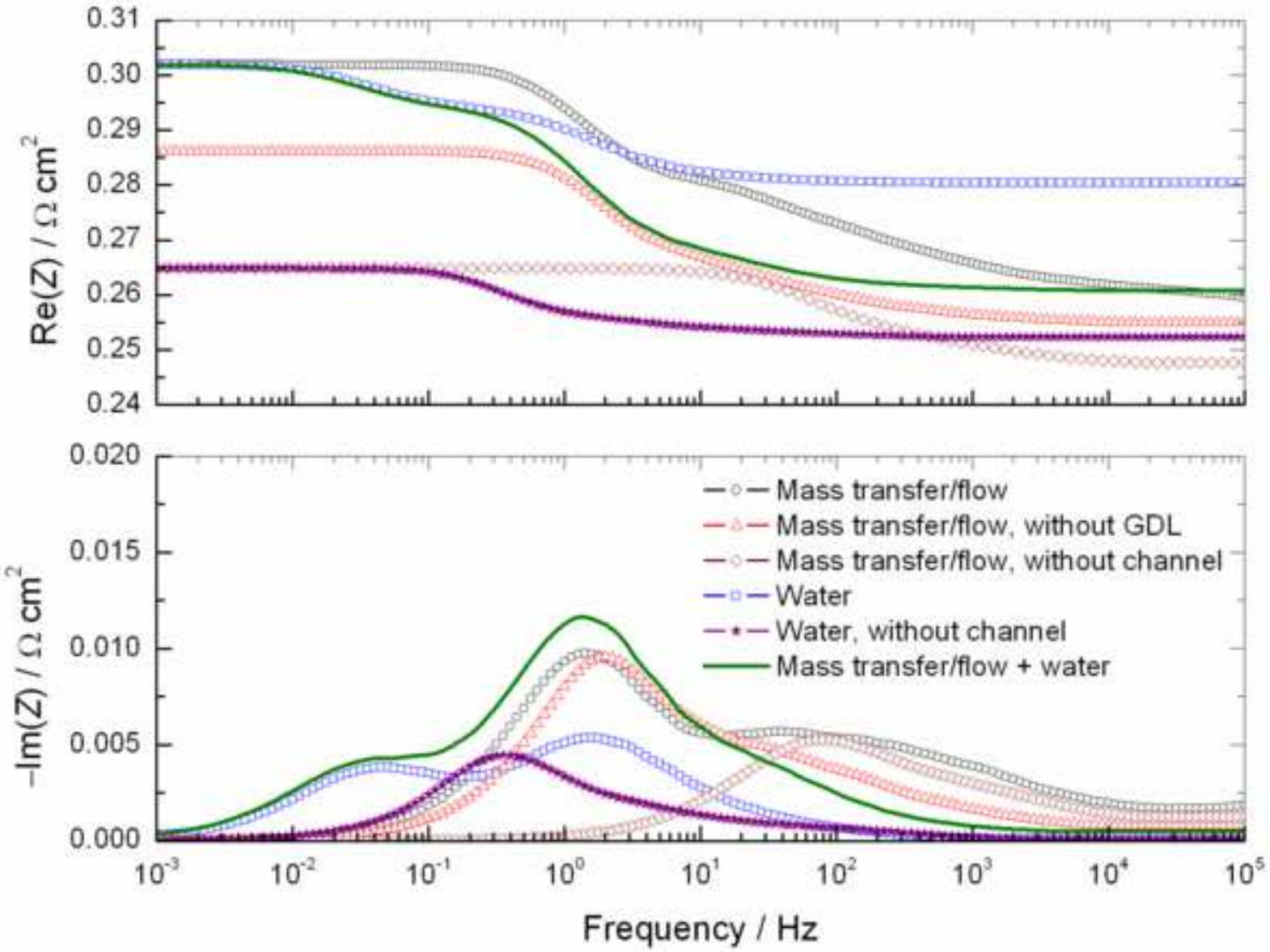

Figure 5b

Click here to download high resolution image

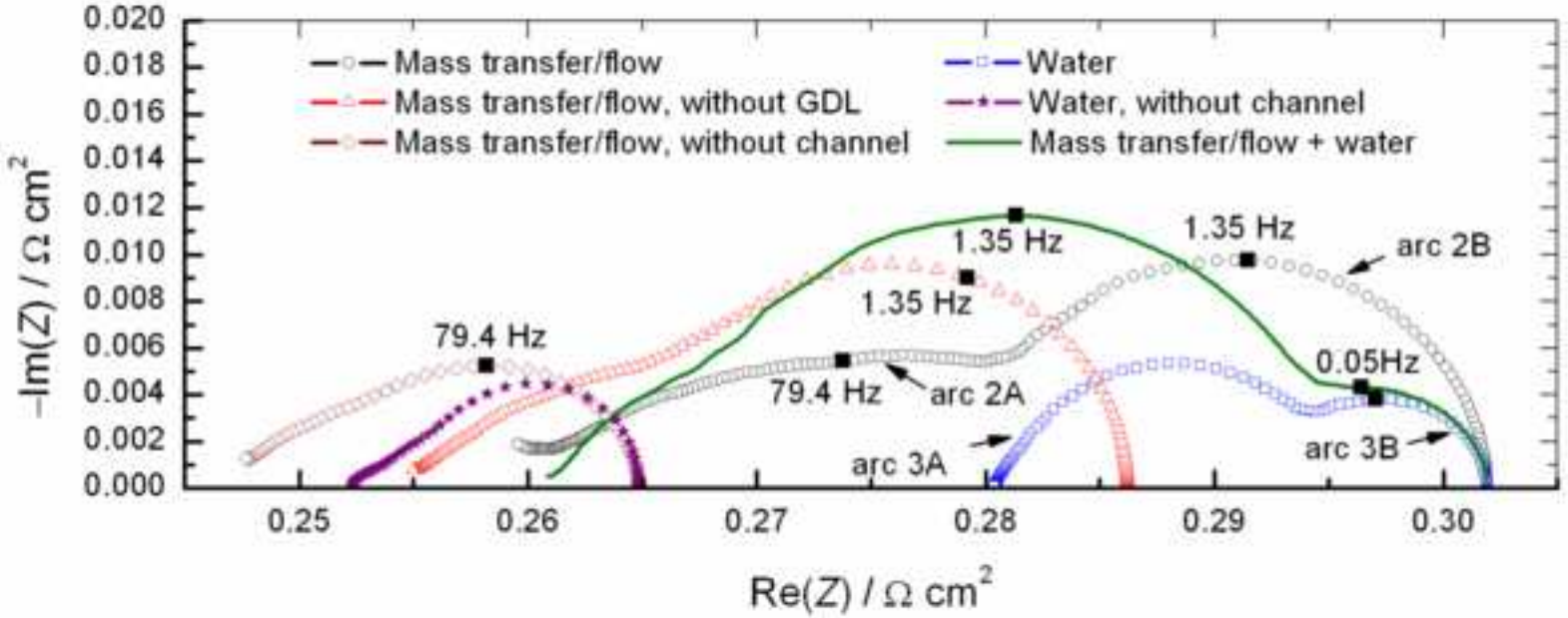

Figure 6a

Click here to download high resolution image

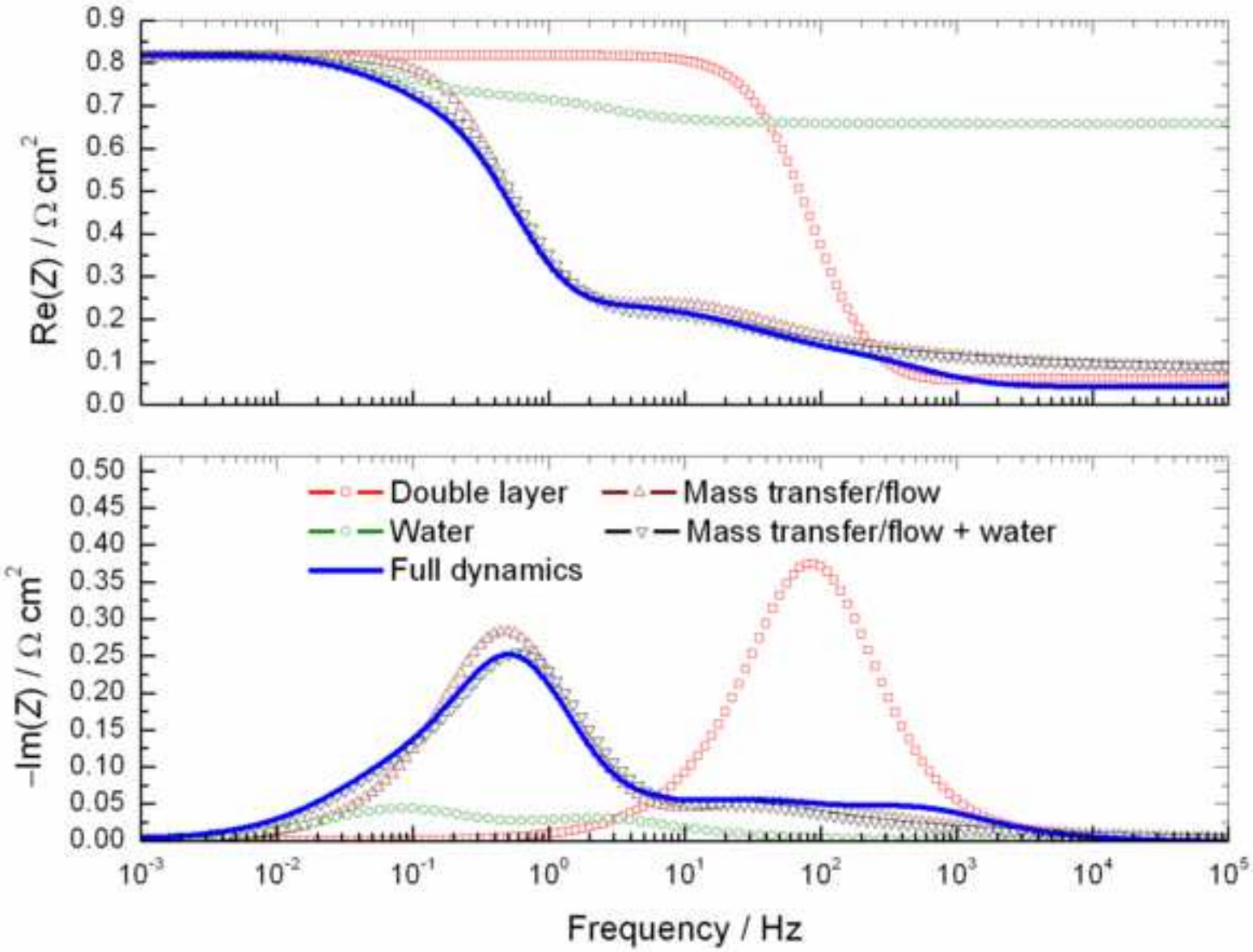

Figure 6b

Click here to download high resolution image

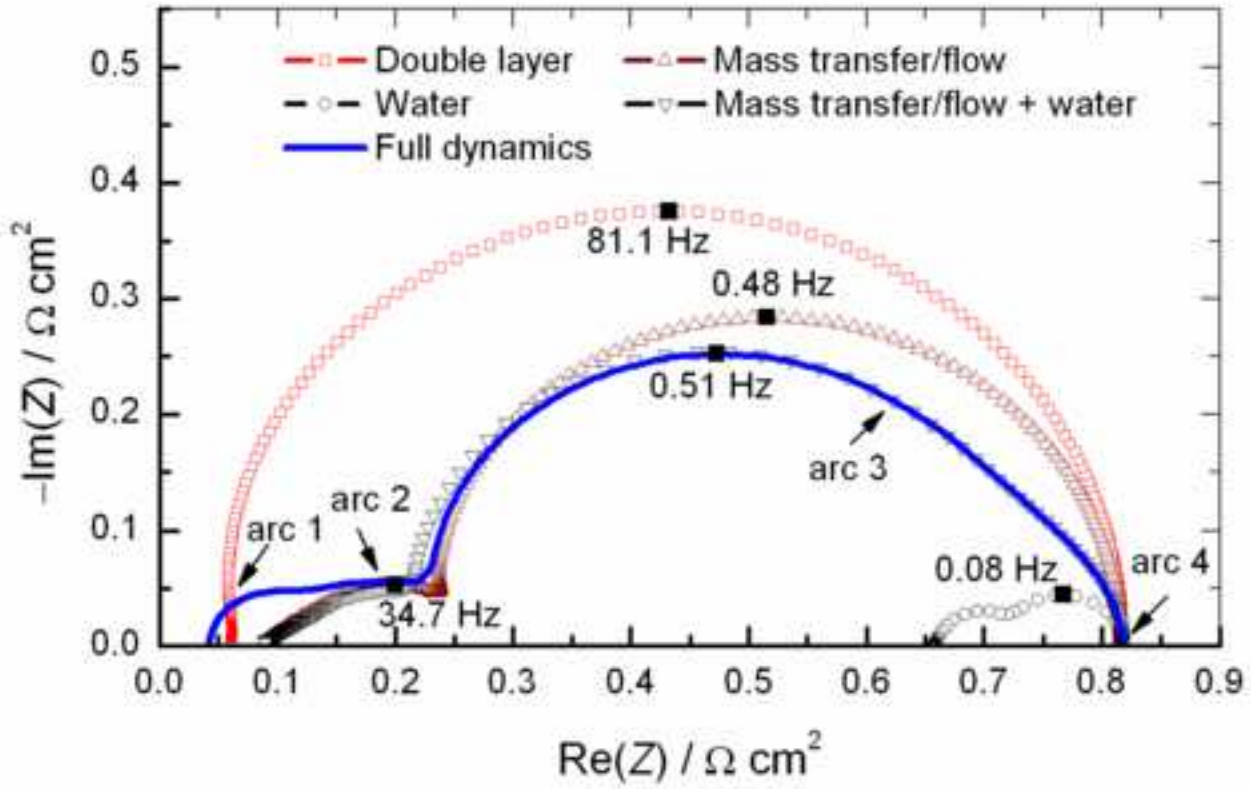

Figure 7

Click here to download high resolution image

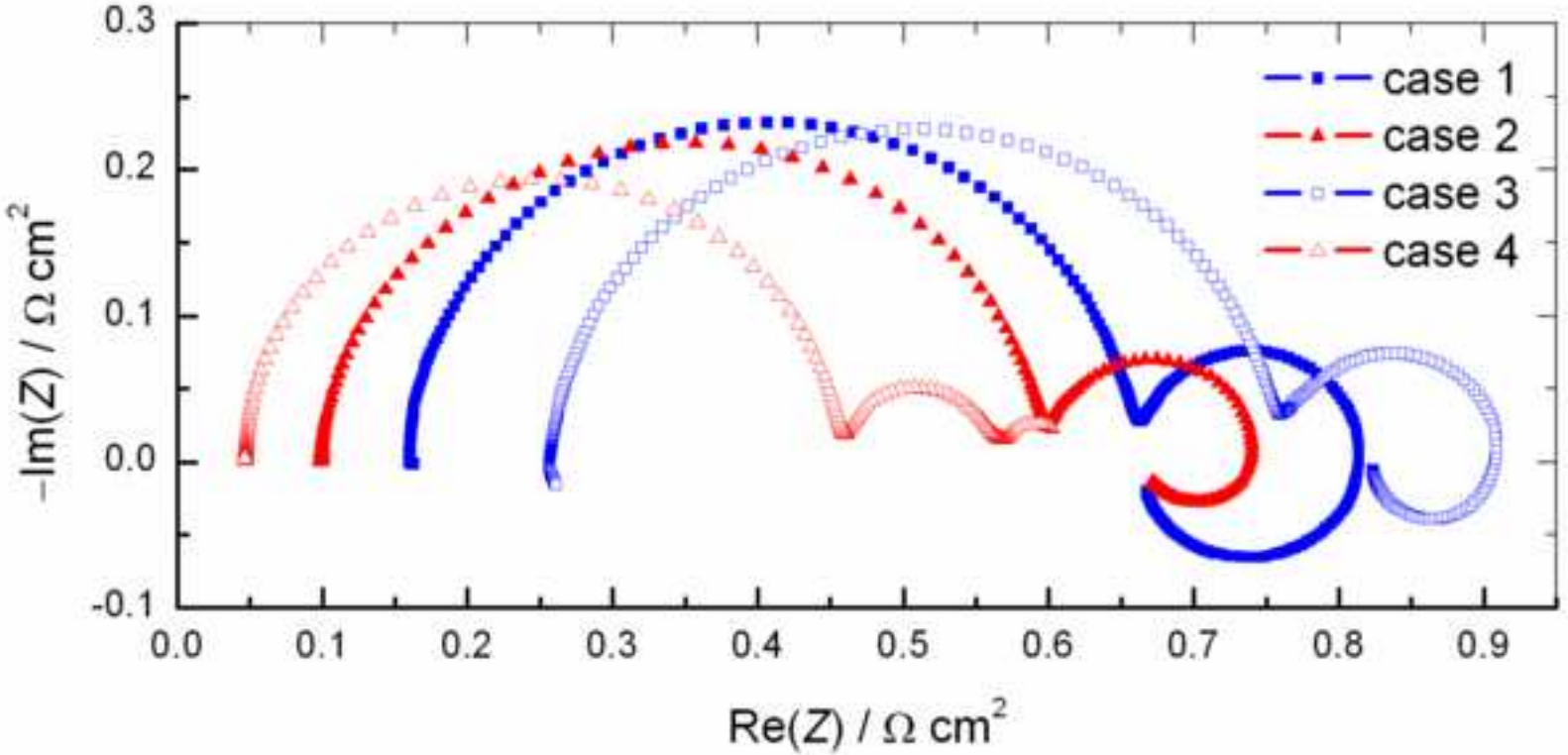

Figure 8a
Click here to download high resolution image

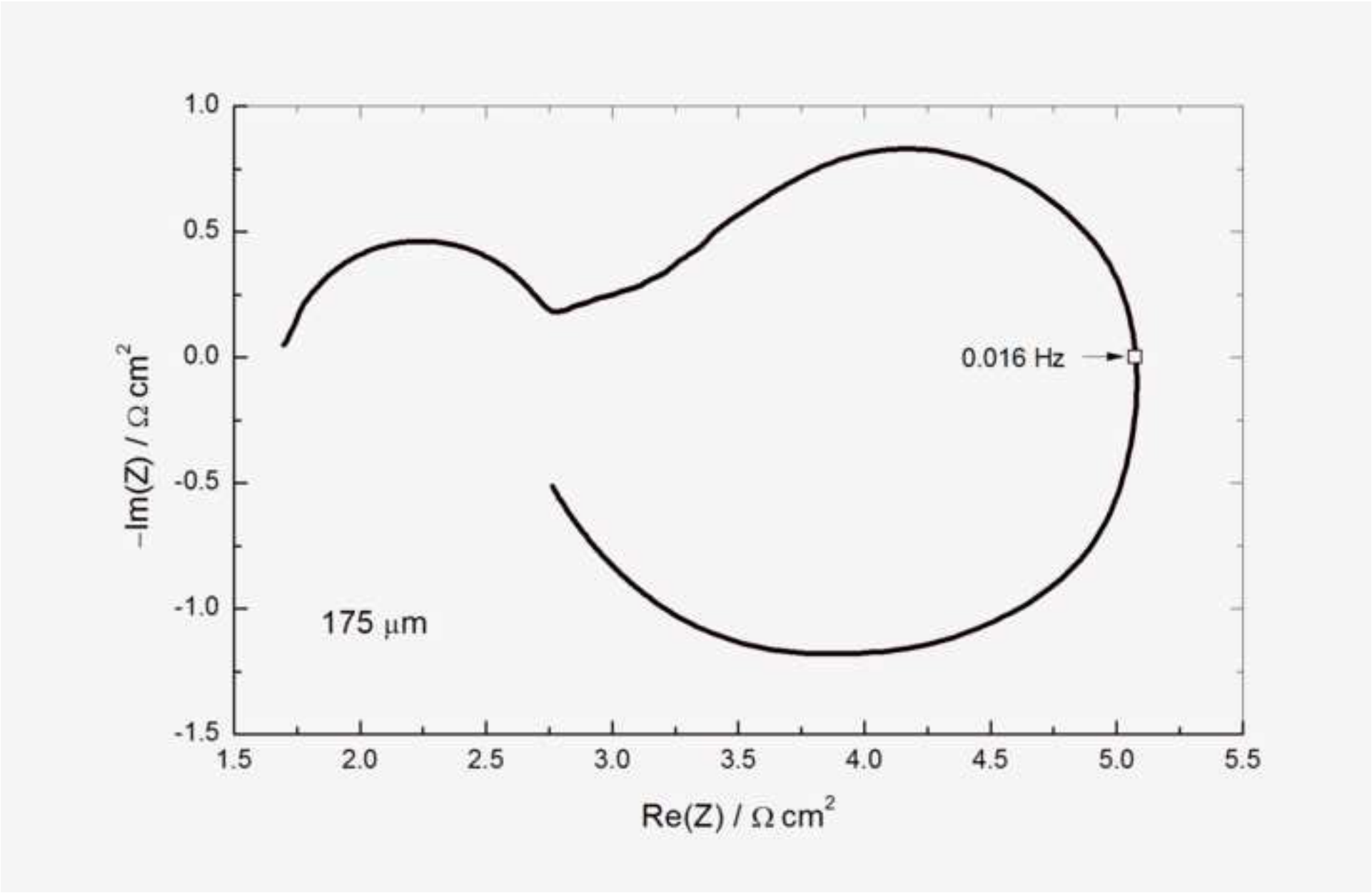

Figure 8b

Click here to download high resolution image